Monthly Notices of the ROYAL ASTRONOMICAL SOCIETY

MNRAS **539,** 3778–3788 (2025) https://doi.org/10.1093/mnras/staf595
Advance Access publication 2025 May 12

Photodissociation of ethanolamine in interstellar clouds driven by UV and soft X-ray irradiation

Heidy M. Quitián-Lara [1,2]★ Jhoan Londoño-Restrepo,[3] Santiago Gómez,[4,5] Kelly V. García-González,[6] Albeiro Restrepo,[4] Nigel J. Mason,[2] Paola Caselli,[1] Heloisa M. Boechat-Roberty [7] and Felipe Fantuzzi [8]

[1]*Max Planck Institute for Extraterrestrial Physics, Gießenbachstraße 1, 85748 Garching, Germany*
[2]*Physics and Astronomy, School of Engineering, Mathematics and Physics, University of Kent, Park Wood Rd, Canterbury CT2 7NH, UK*
[3]*Instituto de Física, Universidad de Antioquia UdeA, Calle 70 No. 52-21, Medellín, 050010, Colombia*
[4]*Instituto de Química, Universidad de Antioquia UdeA, Calle 70 No. 52-21, Medellín 050010, Colombia*
[5]*Department of Physics, Chemistry and Biology (IFM), Linköping University, Linköping SE-581 83, Sweden*
[6]*Departamento de Química, Universidad de Nariño, Calle 18 Cr 50, San Juan de Pasto, 52001, Colombia*
[7]*Observatório do Valongo, Universidade Federal do Rio de Janeiro, Rio de Janeiro, RJ 20080-090, Brazil*
[8]*Chemistry and Forensic Science, School of Natural Sciences, University of Kent, Park Wood Rd, Canterbury CT2 7NH, UK*

Accepted 2025 April 3. Received 2025 March 22; in original form 2025 January 25

ABSTRACT

We investigate the photoinduced fragmentation of ethanolamine (EtA, C_2H_7NO), a prebiotically relevant amino alcohol detected in G+0.693–0.027, under ultraviolet (UV) and soft X-ray irradiation (12–310 eV) to explore its stability and chemical pathways in astrophysical environments. Experimental data were combined with Born–Oppenheimer molecular dynamics simulations, which revealed dominant fragmentation pathways and identified nitrogen-containing species as the major ionic products. Notably, $CH_2NH_2^+$, a highly stable cation formed via C–C bond cleavage and charge localization on the nitrogen centre, emerged as a key fragment. While $CH_2NH_2^+$ has not yet been detected in the interstellar medium, our results indicate it as a promising candidate for future astronomical searches. Calculated photoionization and photodissociation cross-sections enabled the estimation of photodissociation rates and half-lives for EtA under the X-ray conditions of Sgr B2. EtA exhibited a half-life on the order of 10^7 yr, comparable to other complex organic molecules like methyl formate ($HCOOCH_3$) and acetic acid (CH_3COOH) but shorter than simpler molecules such as formic acid (HCOOH). These findings reinforce EtA as a key astrochemical molecule with significant potential for astrobiological implications.

Key words: astrochemistry – molecular processes – radiation mechanisms: general – methods: laboratory: molecular – ISM: clouds – ISM: molecules.

1 INTRODUCTION

Ethanolamine (EtA, 2-aminoethanol, C_2H_7NO; Fig. 1 left), the simplest amino alcohol with separate functional groups, has emerged as a molecule of significant interest in astrobiology and prebiotic chemistry due to its versatile biochemical functionality as both an amine and an alcohol (Bakovic, Fullerton & Michel 2007). In living organisms, it serves as a precursor to phosphatidylethanolamine (Fig. 1 right), a key phospholipid component, through pathways involving intermediates such as phosphatidylserine and ethanolamine phosphate (Nandedkar 1974, 1975; Shukla & Turner 1980). Phosphatidylethanolamine plays a critical role in forming cellular membranes, providing the compartmentalization necessary for cellular processes. Beyond its role in membranes, ethanolamine is integral to biosynthetic pathways for amino acids like glycine ($C_2H_5NO_2$) and more complex quaternary amines such as choline ($C_5H_{14}NO^+$), which itself is a precursor to acetylcholine ($C_7H_{16}NO_2^+$), an essential neurotransmitter in biological systems (Monnard & Deamer 2002; Budin & Szostak 2011). In bacteria, ethanolamine utilization typically involves its cleavage into ammonia and acetaldehyde, which is further converted into acetyl-CoA. Both encapsulated and non-encapsulated pathways of ethanolamine metabolism have been observed (Krysenko et al. 2019), these variations emphasizing its adaptability across evolutionary diverse taxa and its ecological significance.

The prebiotic relevance of ethanolamine has been reinforced by experimental studies demonstrating its potential to form glycine under simulated Archean hydrothermal vent conditions. In such environments, characterized by high temperatures (80–160°C), alkaline pH (ca. 9.7), and anaerobic conditions, ethanolamine reacts efficiently to form glycine in the presence of metal powders under mild pressure (0.1–8.0 MPa). These conditions replicate those hypothesized for early Earth's submarine hydrothermal systems, where H_2 and CO_2

★ E-mail: heidyql@mpe.mpg.de

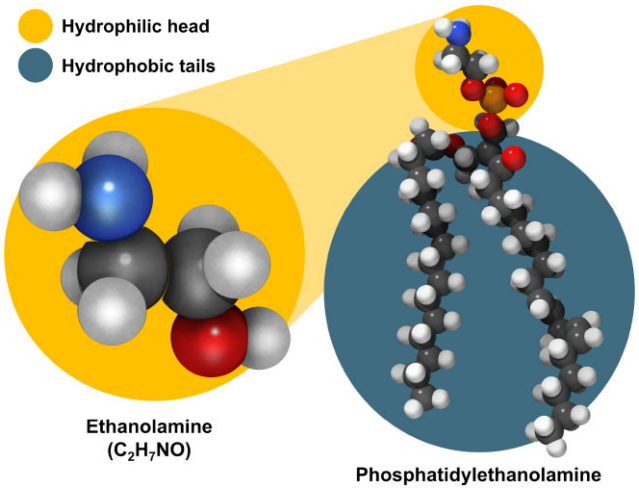

Figure 1. Left: molecular structure of ethanolamine in one of its gas-phase conformations. Right: the phosphatidylethanolamine 1-hexadecanoyl-2-(9*Z*,12*Z*-octadecadienoyl)-*sn*-glycero-3-phosphoethanolamine (Facchini et al. 2016), a key membrane phospholipid. Its hydrophilic head and hydrophobic tails are highlighted in the yellow (left, top right) and blue (bottom right) circles, respectively.

were abundant (Zhang et al. 2017). This reaction not only underscores the importance of high-temperature alkaline hydrothermal vents in the prebiotic synthesis of essential biomolecules but also highlights the role of ethanolamine as a potential precursor to early amino acid formation.

Ethanolamine also shows promise as a precursor to alanine ($C_3H_7NO_2$) through gas-phase reactions under interstellar medium (ISM) conditions. The reaction of protonated ethanolamine with formic acid (HCOOH) has been proposed to produce β-alanine (Ehrenfreund & Charnley 2001). This pathway aligns with theoretical models suggesting that interstellar environments could foster the abiotic synthesis of amino acids and their precursors through radical–radical reactions and catalytic processes on dust grains (Sorrell 2001; Knowles, Wang & Bowie 2010; Ioppolo et al. 2020; Schneiker et al. 2021; Marks et al. 2023; Wang et al. 2024). Such processes are particularly relevant in dense molecular clouds, where molecules are exposed to energetic photons and cosmic rays that facilitate these transformations.

Due to its biological and chemical utility, the potential for ethanolamine to have been delivered to the early Earth by exogenous sources is particularly intriguing. Meteoritic and cometary delivery is a well-studied mechanism for supplying prebiotic compounds to terrestrial environments (Glavin et al. 2010; Burton et al. 2012; Glavin et al. 2012). Indeed, ethanolamine has been detected in the Almahata Sitta meteorite (Glavin et al. 2010), suggesting that amino alcohols could have been synthesized in extraterrestrial environments. Once deposited on a primitive Earth, such molecules could have paved the way for more complex biomolecular assemblies, including phospholipid membranes and peptide chains.

In tandem with its detection in meteoritic materials, the discovery of ethanolamine in the ISM has provided compelling evidence for the widespread distribution of this molecule in space. Recent observations toward the G+0.693–0.027 molecular cloud, a chemically rich region within the Sgr B2 complex near the Galactic Centre, have confirmed the presence of ethanolamine (Rivilla et al. 2021). This finding places C_2H_7NO among a growing list of complex organic molecules (COMs) identified in the central molecular zone (CMZ). The CMZ is known for its harsh physical conditions, including elevated cosmic-ray fluxes, strong X-ray fields, and occasional UV radiation, all of which can drive both the formation and destruction of complex molecules.

Given the formidable conditions within G+0.693–0.027, a major question remains how ethanolamine can persist in environments subjected to intense radiation. Star-forming regions often expose molecules to UV photons emanating from stellar sources, while X-rays produced by accreting objects and cosmic-ray interactions can penetrate deeply into dense clouds (Garrod, Weaver & Herbst 2008; Muñoz Caro et al. 2019). These radiative processes can break molecular bonds or ionize the species, leading to cascading reactions that produce both simpler fragments and new, more complex products (Sandford et al. 2020). Understanding how ethanolamine responds to these radiation fields is thus essential for modelling its survival time-scales and potential to transform into related biomolecules such as glycine or choline.

Laboratory ice-irradiation experiments have emerged as a particularly fruitful approach for investigating the chemical pathways of ethanolamine under interstellar conditions. Through the deposition of ethanolamine-containing ices at cryogenic temperatures (10–100 K) and exposing them to electrons, ions, UV photons, or X-rays, it is possible to simulate the key energetic processes occurring on dust grains in cold, dense regions of the ISM (Biancalani et al. 2024; Ramachandran et al. 2024; Zhang et al. 2024). In these ices, ethanolamine may remain intact to varying degrees, or it may undergo partial or complete dissociation into radicals and ions. Subsequent chemical reactivity can then lead to the synthesis of larger organics or contribute to the formation of new functional groups.

Previous studies have addressed the photochemistry of amino acids, hydrocarbons, and other small organic molecules in astrophysical ice analogues (Bernstein et al. 2002; Gerakines, Moore & Hudson 2004; Holtom et al. 2005; Bennett & Kaiser 2007; Elsila et al. 2007; Pilling et al. 2012; Linnartz, Ioppolo & Fedoseev 2015; Turner et al. 2018; Abplanalp & Kaiser 2019; Eckhardt et al. 2019; Muñoz Caro et al. 2019; Kleimeier, Eckhardt & Kaiser 2021; Cuppen, Linnartz & Ioppolo 2024). Yet, the photodissociation pathways of ethanolamine, especially under combined UV and soft X-ray irradiation, remain insufficiently characterized. When such high-energy photons impact icy grains, they can initiate a range of processes: from the desorption of intact ethanolamine to the production of partially dehydrogenated species or other daughter ions.

The dynamical environment of G+0.693–0.027 further complicates these processes. This region, characterized by large-scale, low-velocity shocks, cloud–cloud collisions, and anomalously high cosmic-ray fluxes (Zeng et al. 2020; Busch et al. 2022; Massalkhi et al. 2023), provides multiple channels for the non-thermal desorption of ethanolamine from grain mantles into the gas phase. Once in the gas phase, ethanolamine encounters intense radiation that can lead to photofragmentation. Consequently, a delicate balance arises between grain-surface formation and preservation of the molecule versus post-desorption photodestruction. Studies aiming to quantify the abundance of ethanolamine in star-forming clouds must therefore incorporate both ice-phase and gas-phase destruction pathways.

The present work focuses on investigating the photoionization and photodissociation of ethanolamine in the gas phase using synchrotron radiation over a wide energy range (12–310 eV). Through a combination of experimental data with *ab initio* molecular dynamics simulations, we examine the mechanisms underlying ethanolamine fragmentation and identify the dominant bond cleavage pathways. This approach allows us to estimate key parameters such as X-ray photoionization and photodissociation cross-sections,

which are subsequently used to calculate the photodissociation rate of ethanolamine under astrophysical conditions. These rates are further employed to estimate its half-life in Sgr B2, providing comparisons with other astrophysically relevant molecules like HCOOH (Boechat-Roberty, Pilling & Santos 2005), methyl formate ($HCOOCH_3$; Fantuzzi et al. 2011), and acetic acid (CH_3COOH; Pilling, Santos & Boechat-Roberty 2006).

2 METHODS

Experimental data for ethanolamine were obtained at the National Synchrotron Light Laboratory (LNLS) facilities in Campinas, Brazil. UV photons above the ionization energy of EtA (8.96 eV, Molder, Pikver & Koppel 1983; calcd. 8.94 eV, Kechoindi et al. 2024) were used, specifically at energies of 12.0, 13.6, 15.5, 17.0, 19.0, 21.0, 100.0, and 200.0 eV. In addition, photons in the soft X-ray range at 288.5, 295.0, 297.5, 300.0, 305.0, and 310.0 eV were also used. The photons were collected at the toroidal grating monochromator (TGM) beamline (Cavasso Filho et al. 2005). EtA, with a purity greater than 99 per cent, was purchased from Merck and injected directly without further purification.

The EtA sample was introduced into the gas phase by simple vaporization inside an ultra-high vacuum chamber, with a base pressure of $\simeq 2.0\times10^{-9}$ mbar. The injection was performed through a capillary with an internal diameter of 0.8 mm, without heating, to avoid sample degradation. The injection process was controlled manually using an analogue valve until a pressure of $\simeq 10^{-6}$ mbar was reached. The injection pressure was kept constant throughout the experiment, ensuring the single collision regime for photon–molecule interactions.

Inside the chamber, the photons passed perpendicularly through the gas-phase sample, which was introduced as a continuous jet. The alignment of the injection needle with the photon beam was verified by recording the emerging beam with a light-sensitive diode. The photons used in this experiment, both UV and X-ray, enabled the analysis of the behaviour of ethanolamine across the range of excitation and ionization energies, both before and after the resonance of the C1s shell. The incident photon flux on the sample was approximately 10^{23} photons s^{-1}, with an energy resolving power of $E/\Delta E > 3000$ (Boechat-Roberty et al. 2009).

For the acquisition of UV data in the 12–21 eV photon energy range, we employed a Ne gas filter to effectively suppress high-order harmonic contamination from the synchrotron beamline, as described by Cavasso Filho et al. (2007). The neon filter was placed in a designated beamline section and operated under a pressure of approximately 0.5 mbar, achieving a suppression efficiency exceeding 99.9 per cent for photon energies below the ionization threshold of Ne (21.5 eV), thereby enhancing the reliability and precision of our measurements.

For the analysis of the ionized species, a Wiley and McLaren time-of-flight mass spectrometer (TOF-MS) was used. Ionized species produced by the interaction of the photon beam were accelerated and focused by a two-stage electric field, passing through a 297 mm-long fieldless drift tube, and finally detected by a pair of microchannel plate (MCP) detectors arranged in a chevron configuration. A high voltage of 4250 V applied to the front of the MCP ensured independence of the detection efficiencies with respect to the mass and charge states of the ions. The photoelectrons, accelerated in the opposite direction to the positive ions, were focused by an electrostatic lens system and detected by another pair of MCP detectors arranged in the same configuration. A DC electric field of 500 V cm^{-1} was applied to the first stage of ion acceleration. Electrons with initial kinetic energies up to 150 eV and ions up to 30 eV were detected without energy analysis.

During the experiments, photoelectron and photoion coincidence spectra (PEPICO) were collected, where each ejected photoelectron was recorded in coincidence with its respective cation. The start (photoelectron) and stop (photoion) signals were correlated, converted from the time domain (nanosecond range) to the mass-to-charge ratio (m/q) domain, and expressed in terms of intensity as a function of m/q, resulting in PEPICO mass spectra. Calibration of the TOF spectrometer was carried out by identifying the most abundant peaks in the sample mass spectra and comparing them with data from the National Institute of Standards and Technology database (NIST, William 2025).

We determined the partial ionic yield (PIY per cent) for each fragment observed in the mass spectra using the following equation:

$$PIY(\%) = \left[\frac{A_i^+}{\sum A_i^+}\right] \times 100. \quad (1)$$

In this equation, A_i^+ represents the area of each ion i, obtained through a simple Gaussian fit, while $\sum A_i^+$ denotes the total area of all peaks in the PEPICO spectrum. The A_i^+ values were corrected for ion and electron detection efficiencies, following the methodology described by Burmeister et al. (2010) for the same TOF-MS and detector set-up.

The PIY is expressed as a percentage, with uncertainties estimated to be approximately 10 per cent for the largest peak areas and up to 15 per cent for the smallest ones. Furthermore, the uncertainty in the peak position is estimated at $\pm$0.5 m/q. It should be noted that the resolution of our spectrometer is 1 amu. Consequently, some masses may encompass multiple overlapping contributions.

To simulate the fragmentation pathways of EtA, we utilized the QCxMS package (Bauer & Grimme 2016; Koopman & Grimme 2021). This software performs conformational sampling via Born–Oppenheimer molecular dynamics (BOMD), generating snapshots that serve as initial structures for a specified number of fragmentation dynamics simulations. The GFN2-xTB Tight Binding method (Bannwarth, Ehlert & Grimme 2019; Bannwarth et al. 2021) was employed as the Hamiltonian to describe the electronic structure during molecular fragmentation. This method has demonstrated reliable accuracy in a broad range of organic and inorganic molecules (Ásgeirsson, Bauer & Grimme 2017; Koopman & Grimme 2019).

A total of 24 000 dissociation dynamics were simulated from the selected snapshots, comprising 6000 runs each for durations of 16, 50, 100, and 150 ps, with an integration time-step of 0.25 fs. The impact ionization energy was set to 288 eV, corresponding both to the resonance energy of the 1*s* electrons of carbon atoms in EtA and to the lower limit of photon impact energies in the X-ray experiments. As such, the intensities in the reported simulated spectra are expected to provide a robust description of the experimental results.

3 RESULTS AND DISCUSSION

Sections 3.1 and 3.2 explore the PIY production from EtA for UV and soft X-ray photons, respectively, with the corresponding spectra and m/q attributions presented in Fig. 2, and the PIY data summarized in Table 1. Section 3.3 highlights the main fragmentation mechanisms derived from BOMD results, while Section 3.4 focuses on the determination of absolute photoionization and photodissociation cross-sections. Finally, Section 3.5 evaluates the half-life of EtA in Sgr B2, drawing comparisons with selected organic molecules.

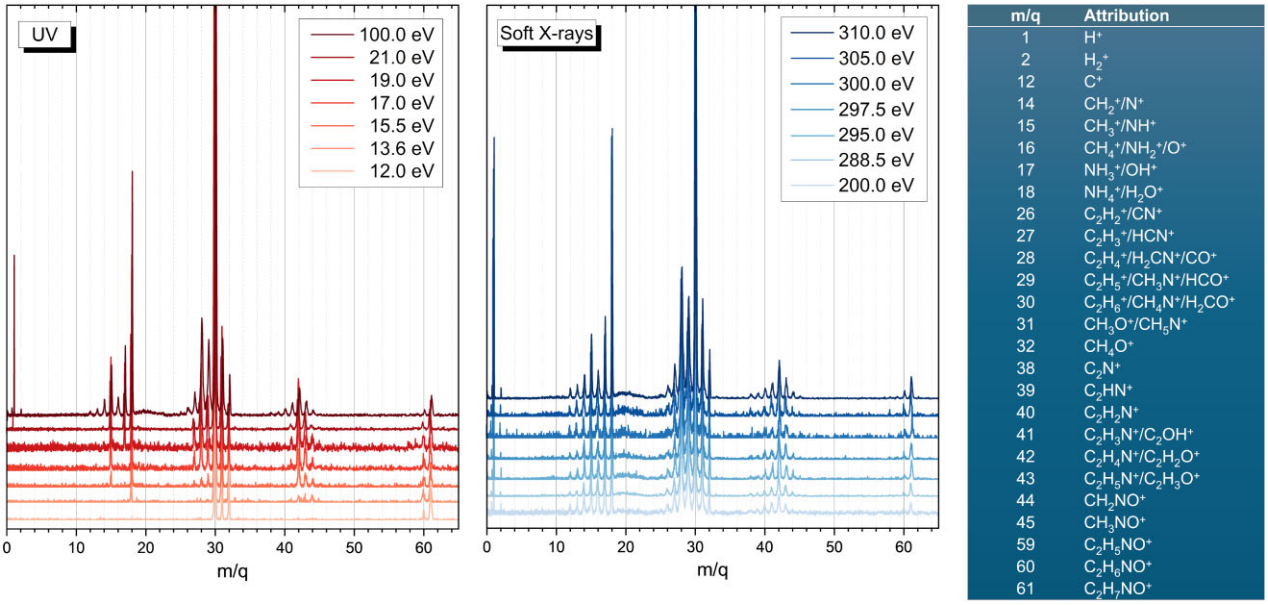

Figure 2. Ethanolamine mass spectra recorded using UV photons (left panel) and soft X-rays (centre panel). The right panel presents the attribution of the distinct m/q fragments detected in the experiments, considering all plausible assignments based on the stoichiometry of the parent molecule (C_2H_7NO). Fragment ions corresponding to H_nNO^+ (n = 0–2) for m/q = 30–32 were not considered, as nitrogen and oxygen occupy extreme positions in the molecule, making the formation of such ions less likely.

Table 1. Partial ion yield (per cent), as a function of photon energy in the UV and X-ray ranges. For m/q attributions, see Fig. 2. At 200.0 eV, the lower resolution compared to other X-ray photon energies prevented the detection and quantification of the ion with m/q = 60.

m/q	*PIY* (per cent), per energy (eV)													
	12.0	13.6	15.5	17.0	19.0	21.0	100.0	200.0	288.5	295.0	297.5	300.0	305.0	310.0
1						8.48	10.09	3.94	11.46	12.66	12.32	12.37	12.40	13.20
2						0.37	0.41	0.12	0.44	0.53	0.69	0.52	0.63	0.61
12						1.05	1.22	1.21	0.47	0.49	0.62	0.72	0.63	0.71
14								2.34	1.58	1.97	1.87	1.50	2.06	1.75
15				3.76	4.76	3.88	3.49	4.14	3.69	3.56	3.77	4.05	3.57	3.76
16						1.38	1.70	5.77	1.99	1.80	2.02	2.03	2.36	2.12
17					2.35	3.53	3.64	6.46	3.57	3.64	3.73	3.88	3.56	3.53
18				7.53	6.81	9.14	9.55	12.40	8.91	8.12	8.20	8.86	8.21	8.54
26								2.04	1.00	0.96	0.96	0.69	0.97	0.92
27				1.18	1.93	1.72	1.81	3.39	2.44	2.61	2.40	2.45	2.86	2.57
28				3.50	4.88	10.04	11.11	11.42	10.99	9.86	10.90	9.79	11.24	10.82
29				2.34	3.38	7.48	8.27	8.73	7.88	10.10	7.84	7.50	8.47	8.25
30	80.25	80.23	76.84	60.18	55.13	36.88	31.60	21.72	29.84	28.63	28.53	29.56	27.93	27.81
31	4.91	9.70	7.60	7.65	6.59	5.75	5.01	5.31	4.99	5.13	5.41	5.68	5.07	4.91
32	7.06	3.63	3.04	2.56	2.38	1.80	1.68	1.80	1.85	1.73	1.64	1.48	1.91	1.68
38								0.76	0.40	0.16	0.32	0.31	0.44	0.34
39							0.51	0.62	0.39	0.30	0.39	0.41	0.33	0.40
40						0.49	0.88	1.12	0.77	0.68	0.86	0.81	0.72	0.77
41						1.02	1.54	1.56	1.23	0.78	1.16	0.96	1.27	1.17
42		0.72	4.90	4.70	0.81	3.17	3.45	2.37	2.62	2.68	2.52	2.78	2.62	2.49
43		0.40	2.38	2.47	4.77	1.54	1.82	1.36	1.46	1.46	1.36	1.49	1.22	1.28
44		0.75	1.13	0.96	2.44	0.44	0.68	0.64	0.51	0.35	0.44	0.34	0.34	0.42
45									0.15	0.14	0.13	0.33	0.10	0.11
59											0.14	0.15	0.10	0.12
60	0.90	1.53	1.35	1.02	1.18	0.40	0.31		0.30	0.41	0.33	0.30	0.33	0.39
61	6.87	3.03	2.77	2.17	2.57	1.43	1.22	0.77	1.09	1.18	1.21	0.94	1.09	1.09

3.1 PEPICO: UV energies

The left panel of Fig. 2 shows the fragmentation patterns of EtA as a function of photon energy in the UV range. Fragmentation begins at 12.0 eV, above the first ionization potential (8.96 eV, Molder et al. 1983; calcd. 8.94 eV, Kechoindi et al. 2024), with low production of ion families, and intensifies with increasing photon energy (Table 1). Among the observed fragments, the ion with m/q = 30, corresponding to the base peak ($C_2H_6^+/CH_2O^+/CH_4N^+$), is the most abundant at all energies. Despite its PIY decreasing significantly

from 80.25 per cent at 12.0 eV to 31.60 per cent at 100.0 eV, it remains the dominant fragment, highlighting its central role in the dissociation dynamics at all experimental energies. In contrast, the ion with m/q = 28 ($C_2H_4^+$/CH_2N^+) exhibits an opposite trend. Its PIY increases steadily with photon energy, starting at 3.50 per cent at 17.0 eV, rising to 4.88 per cent at 19.0 eV, 10.04 per cent at 21.0 eV, and reaching a maximum of 11.11 per cent at 100.0 eV.

Other significant fragments include m/q = 18, m/q = 1, m/q = 29, m/q = 31, m/q = 15, and m/q = 17. The fragment m/q = 18, attributed to NH_4^+/H_2O^+, exhibits an increasing trend, starting at 7.53 per cent at 17.0 eV and rising to 9.55 per cent at 100.0 eV. The ion m/q = 1 (H^+), representing a high yield of free protons, becomes significant at 21.0 eV, with its photoionization yield (PIY) increasing from 8.48 per cent at 21.0 eV to 10.09 per cent at 100.0 eV.

The cation m/q = 29 ($C_2H_5^+$/CH_3N^+/HCO^+) shows a notable PIY increase, starting at 2.34 per cent at 17.0 eV and reaching a maximum of 8.27 per cent at 100.0 eV. The fragment m/q = 31, attributed to CH_3O^+/CH_5N^+, begins with a PIY of 4.91 per cent at 12.0 eV, increases at 13.6 eV, and then declines slightly to 5.01 per cent at 100.0 eV. Fragments m/q = 15 (CH_3^+/NH^+) and m/q = 17 (NH_3^+/OH^+) exhibit similar abundances, reflecting comparable contributions across the energy range.

Regarding the parent ion, m/q = 61 ($C_2H_7NO^+$) shows a steady decrease in abundance with increasing energy. Its PIY declines from 6.87 per cent at 12.0 eV to 1.22 per cent at 100.0 eV, indicating efficient destruction of EtA within this energy range. This finding is consistent with the breakdown diagram in the 9.20–9.80 eV energy range reported by Kechoindi et al. (2024), which shows strong production of m/q = 30 after approximately 9.57 eV and low survivability of m/q = 61 beyond 9.70 eV.

3.2 PEPICO: soft X-rays

The EtA fragmentation patterns as a function of photon energy in the soft X-ray region (Fig. 2, right panel), particularly around the C1s resonance, reveal dissociation dynamics comparable to those observed at UV energies. While fragmentation intensities between 200.0 eV and 310.0 eV exhibit slight variations in PIYs, the exclusive production of m/q ions 14, 26, 38, 45, and 59 at soft X-ray energies highlights the opening of new fragmentation channels under these conditions (Table 1).

The ion with m/q = 30 ($C_2H_6^+$/CH_4N^+/H_2CO^+) remains dominant at all photon energies, consistently serving as the base peak. Its PIY starts at 21.72 per cent at 200.0 eV, increases slightly to a maximum of 29.84 per cent at 288.5 eV, and stabilizes between 28 and 29 per cent at higher photon energies, underscoring its central role in the dissociation dynamics of ethanolamine. The second most abundant ion, m/q = 28 ($C_2H_4^+$/CH_2N^+), exhibits a stable, slightly increasing trend across the energy range. Its PIY begins at 11.42 per cent at 200.0 eV, fluctuates between 9.79 per cent and 11.24 per cent at intermediate energies, and reaches 10.82 per cent at 310.0 eV.

The ion H^+ shows significant growth, with its PIY starting at 3.94 per cent at 200.0 eV and rising to a peak of 13.20 per cent at 310.0 eV. This stability near its peak could suggest a tendency towards maximum deprotonation above the C1s resonance. Other fragments display intermediate abundances, including m/q = 29 ($C_2H_5^+$/CH_3N^+/HCO^+), which exhibits moderate production with PIY values ranging from 10.10 per cent to 7.50 per cent. The fragment m/q = 17 (NH_3^+/OH^+) maintains an almost constant abundance of around 3.6 per cent. Similarly, m/q = 31 (CH_3O^+/CH_5N^+) shows consistent production across the energy range, fluctuating between 4.91 per cent and 5.68 per cent without significant energy dependence.

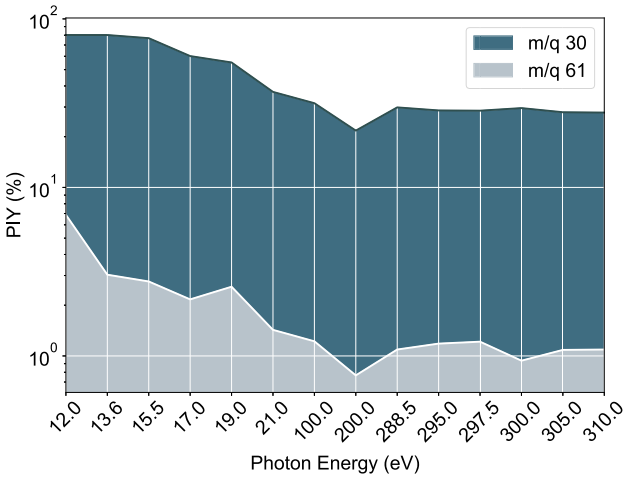

Figure 3. Partial ion yield (per cent) of m/q = 30 and m/q = 61 as a function of photon energy across the investigated range.

The parent ion (m/q = 61) exhibits a nearly constant PIY of around 1 per cent, while low-abundance fragments such as m/q = 12 (C^+) and m/q = 26 ($C_2H_2^+$) remain below 2 per cent at all energies, contributing minimally to the overall fragmentation dynamics.

The fragmentation patterns observed under both soft X-ray and UV valence energies exhibit notable similarities, emphasizing that the fragmentation pathway of the ethanolamine parent ion predominantly favours the production of fragments around m/q = 30. This finding highlights the rapid dissociation of ethanolamine, with minimal variation in the dominance of the base peak as photon energy increases. Fig. 3 illustrates the partial ion yield (PIY, per cent) of the parent ion relative to the base peak across all experimental energies.

Finally, it is important to highlight that in our UV and X-ray mass spectral analyses, no evidence of long-lived dicationic fragments was observed. Typically, such species would appear as very sharp peaks (Monfredini et al. 2016; Fantuzzi et al. 2018; Quitián-Lara et al. 2020) – a signature that is absent in our experiments, as confirmed by the full width at half-maximum (FWHM) values from our Gaussian fits. Furthermore, the PEPIPICO data revealed only sparse double coincidences under UV irradiation and essentially none under soft X-ray conditions. Our theoretical calculations corroborate this experimental observation: at the PBE0-D3(BJ)/def2-TZVP level, the computed vertical second ionization energy of EtA is 27.1 eV, yet subsequent optimization of the dicationic structure invariably leads to rapid C–C bond cleavage into two singly charged fragments. These combined findings confirm that doubly ionized EtA does not persist under the conditions investigated.

3.3 Fragmentation pathways as revealed by BOMD simulations

Given the resolution of our spectrometer, several m/q ratios can correspond to multiple ion candidates due to the overlap of potential fragment ions. For instance, the base peak at m/q = 30, which dominates the fragmentation spectra, can be attributed to three plausible stoichiometries: $C_2H_6^+$, CH_4N^+, and CH_2O^+, each of which may exist in multiple isomeric forms. Identifying the most likely

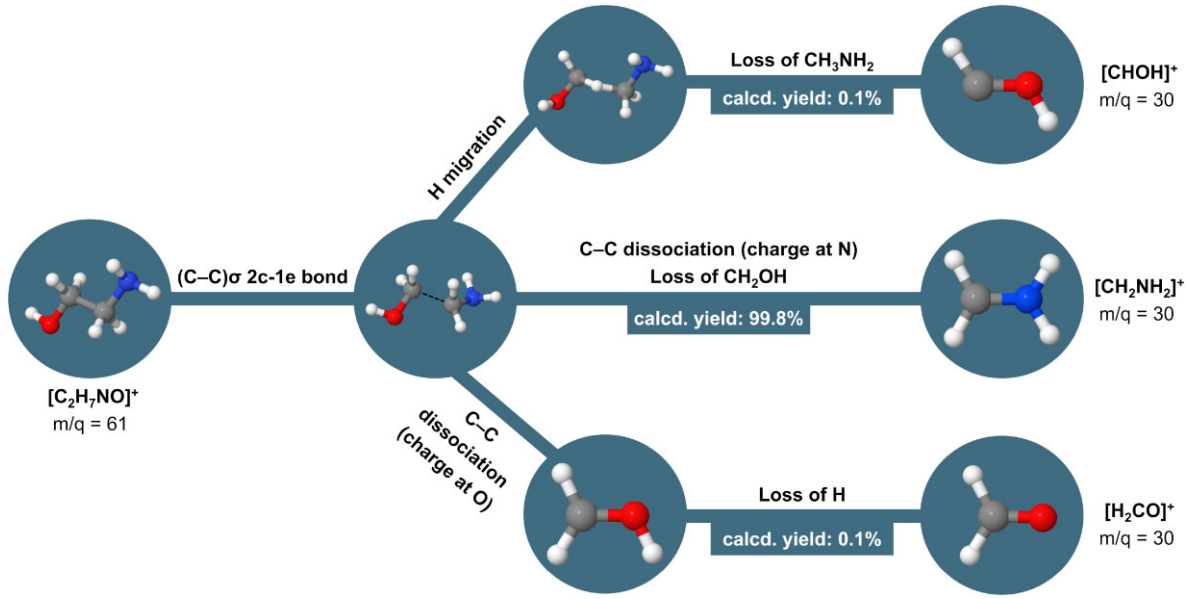

Figure 4. Schematic representation of the primary fragmentation pathways of EtA leading to fragments with $m/q = 30$, based on experimental and computational results. The dominant pathway (centre) involves direct C–C bond cleavage, resulting in the formation of the nitrogen-containing $CH_2NH_2^+$ ion, which dominates the fragmentation spectra. Alternative pathways (top and bottom) produce two distinct CH_2O^+ isomers-*trans*-$CHOH^+$ (top) via hydrogen migration from the CH_2OH group and H_2CO^+ (bottom) through charge localization on the oxygen-bearing fragment after dissociation. All pathways proceed from the elongated C–C bond minimum of EtA^+, as identified by BOMD simulations. The calculated yields of these pathways, expressed as a percentage of the total trajectories leading to m/q = 30 ions, are also indicated.

fragment ions resulting from the photodissociation of EtA is crucial for understanding its dissociation dynamics. To this end, we relied on computational analyses as detailed in Section 2. A comprehensive examination of the simulated spectrum, along with its comparison to experimental data from the NIST database (William 2025) –showing excellent agreement – is presented elsewhere (Londoño-Restrepo et al. 2025). Here, we discuss this data in the context which is relevant for the current investigation. We then focus on the primary fragmentation channels, particularly the base peak at m/q = 30, with the results summarized in Fig. 4.

The dissociation dynamics of EtA demonstrates a clear preference for the initial rupture of the C–C bond. Starting from the neutral structure and following the elongation of this bond, calculations at the MP2/6-311+G(d,p) level reveal two distinct energy minima along the dissociation pathway. The second minimum, characterized by an elongated (C–C)σ 2-centre 1-electron (2c-1e) bond, is lower in energy (Londoño-Restrepo et al. 2025). Notably, 2c-1e bonds have been a topic of recent theoretical interest (de Sousa & Nascimento 2017, 2019; Cardozo et al. 2024) and may also be prevalent in organic radical cations (Fantuzzi et al. 2019; Bonfim et al. 2024; Shimajiri et al. 2024).

From the C–C elongated EtA^+ minimum, three major dissociation pathways emerge. The first involves straightforward C–C bond cleavage (Fig. 4, centre pathway), with the resulting charge localized on the nitrogen-bearing fragment. This process leads to the formation of $CH_2NH_2^+$, observed in 99.8 per cent of simulations where m/q = 30 ions were formed. Interestingly, $CH_2NH_2^+$ plays an essential role in astrochemistry, particularly in the ionosphere of Titan, where it is a significant component. Measurements by the ion neutral mass spectrometer (INMS) on the Cassini spacecraft detected m/q = 30 and attributed it to $CH_2NH_2^+$, formed via proton attachment to methanimine (CH_2NH; Vuitton et al. 2006a; Vuitton, Yelle & Anicich 2006b). Methanimine, known for its high proton affinity, readily accepts a proton to form $CH_2NH_2^+$ (de Oliveira et al. 2001). Alternatively, $CH_2NH_2^+$ can form through hydrogen loss from the thermodynamically more stable methylaminyl cation ($CH_3NH_2^+$; Singh et al. 2010) or by the dissociative photoionization of ethylenediamine (Muller et al. 2016).

The formation of $CH_2NH_2^+$ has been studied extensively since its measurement by Huntress & Elleman (1970), who reported its production via ion–molecule reactions in methane–ammonia (CH_4/NH_3) mixtures, attributed to the rapid reaction of NH_3 with CH_2^+ (Anicich 1993). Additional studies reported its formation through the reaction of NH_3 with the methoxymethyl cation ($CH_3OCH_2^+$; Okada et al. 1987), while its destruction via electron recombination to form NH_2 has been highlighted by Yelle et al. (2010).

Due to its importance in Titan's atmosphere, $CH_2NH_2^+$ has been the focus of theoretical studies by Thackston & Fortenberry (2018) and joint theoretical and experimental investigations by Markus et al. (2019). Although it has not yet been detected in the ISM, modelling studies (Suzuki et al. 2016; Yuen et al. 2019) suggest that the dissociative recombination of $CH_2NH_2^+$ is a key formation route for interstellar CH_2NH, alongside reactions such as NH + CH_3, which is the primary pathway. Additionally, the University of Manchester Institute of Science and Technology database (UMIST, Millar et al. 2024) identifies two distinct pathways for the dissociative recombination of $CH_2NH_2^+$, resulting in the formation of either CH_2NH+ H or CH_2+ NH_2.

More recently, $CH_2NH_2^+$ was identified as a major product of hydrogen-transfer reactions involving H_2CNH^+ and $HCNH_2^+$ with propene, the former ion showing higher reactivity (Richardson et al. 2024). Our findings provide additional evidence for the astrochemical importance of $CH_2NH_2^+$, identifying photodissociation of EtA and related alkylamines (Leclerc & Lorquet 1967) as potential sources. The combined detection of EtA, methylamine (CH_3NH_2;

Zeng et al. 2018) and ethylamine ($C_2H_5NH_2$, Zeng et al. 2021) in G+0.693–0.027, further support the relevance of $CH_2NH_2^+$ as a candidate for interstellar detection, particularly in dense regions where the ionization fraction is relatively low. Collectively, these results highlight the importance of searching for $CH_2NH_2^+$ in these environments.

In addition to $CH_2NH_2^+$, a small fraction of our simulated trajectories led to the formation of two distinct CH_2O^+ isomers (approximately 0.1 per cent each) with m/q = 30. The *trans*-$CHOH^+$ ion was observed in all cases where hydrogen migration occurred from the CH_2OH group of the $C_2H_7NO^+$ ion with an elongated C–C bond (Fig. 4, top pathway). In contrast, the formation of its isomer, H_2CO^+, resulted from direct C–C bond dissociation of the parent ion (Fig. 4, bottom pathway), with the positive charge localized on the oxygen-bearing fragment. This pathway proceeds through the intermediate CH_2OH^+ (m/q = 31), which subsequently undergoes hydrogen loss to yield H_2CO^+.

Notably, CH_2OH^+ was the predominant isomer with m/q = 31, appearing in 94.1 per cent of trajectories that produced ions with this m/q value, and it was the only ion of this stoichiometry observed. The remaining 5.9 per cent of m/q = 31 ions corresponded to the $CH_3NH_2^+$ cation, demonstrating a minor but measurable contribution in the simulated dissociation pathways.

Our simulations make it clear that $CH_2NH_2^+$ is the predominant fragment with m/q = 30, consistent with previous studies (e.g. Kechoindi et al. 2024). Interestingly, the $C_2H_6^+$ cation did not appear in any of our trajectories, indicating that its formation can be confidently excluded under the conditions investigated.

With respect to ions with m/q = 28, the majority of the simulated trajectories (98.1 per cent) resulted in the formation of $HCNH^+$, with only 1.9 per cent attributed to H_2CN^+. This distribution highlights the strong preference for $HCNH^+$ formation under the dissociation conditions investigated. For m/q = 29, the trajectories were predominantly associated with nitrogen-bearing fragments, accounting for 84.4 per cent of the ions formed. Specifically, 46.1 per cent of these were identified as CH_2NH^+, while 38.3 per cent were attributed to $CHNH_2^+$. The remaining 15.6 per cent corresponded to HCO^+, indicating a lesser but still significant contribution from oxygen-bearing fragments.

These results further emphasize the predominance of nitrogen-bearing ionic species in the photodissociation of ethanolamine, reinforcing the role of nitrogen-containing fragments as key intermediates in the dissociation pathways. This finding is consistent with the overall dissociation dynamics of ethanolamine, where the localization of the charge and fragmentation pathways strongly favour nitrogen-containing products.

Our simulations also reveal interesting results for ions with m/q = 41–43. For m/q = 41, 90.2 per cent of the trajectories leading to this value correspond to nitrogen-bearing species. The most abundant nitrogen-containing ion is CH_2CNH^+, accounting for 56.9 per cent of the total, followed by $HCCNH_2^+$ at 33.3 per cent. The only oxygen-bearing ion observed with m/q = 41 was $HCCO^+$, contributing the remaining 9.8 per cent of the trajectories.

For m/q = 42, four distinct species were identified, consisting of two oxygen-bearing and two nitrogen-bearing ions. Nitrogen-bearing species were more prominent, comprising 66.6 per cent of the trajectories. Among these, 37.0 per cent were attributed to $H_2CCNH_2^+$ and 29.6 per cent to CH_3CNH^+. The oxygen-bearing ions were less frequently observed, with 17.6 per cent corresponding to H_2CCO^+ and 15.7 per cent to $HCCOH^+$.

Finally, for m/q = 43, the majority of the trajectories (59.0 per cent) were associated with the vinylamine cation ($C_2H_3NH_2^+$), the singly charged form of a nitrogen-bearing species considered a potential building block of nucleosides and nucleotides. Vinylamine can form in interstellar ice analogues containing acetylene and ammonia when exposed to energetic electrons (Zhang et al. 2023), suggesting it may also play a role in Titan's chemistry (Cable et al. 2018). Oxygen-bearing ions also contributed significantly to m/q = 43 as well, with 25.6 per cent corresponding to H_2CCOH^+ and 15.4 per cent to CH_3CO^+.

Our simulations also captured trajectories resulting in the formation of ions with m/q = 60. Among the six $C_2H_6NO^+$ isomers identified, two accounted for 84.5 per cent of the trajectories. Interestingly, both are associated with the loss of hydrogen from the carbon atoms, with the most abundant isomer (64.5 per cent) forming through hydrogen loss from the carbon atom adjacent to nitrogen. The second most prevalent isomer (24.0 per cent) arises from hydrogen loss from the carbon atom near oxygen. We propose that this behaviour is linked to the reconstruction of the (C–C)σ 2c–2e bond in the elongated $C_2H_7NO^+$ minimum, facilitated by hydrogen atom release.

3.4 Absolute photoionization and photodissociation cross-sections

Having the PIYs of the parent ion and the distinct fragments of EtA for soft X-ray energies at hand, it is possible to estimate the (non-dissociative) photoionization $\sigma_{\text{ph-i}}$ and photodissociation (or dissociative photoionization, $\sigma_{\text{ph-d}}$) cross-sections. However, this requires knowledge of the photoabsorption cross-section $\sigma_{\text{ph-abs}}$ of the molecule as a function of photon energy. To determine this, the absolute photoabsorption cross-section of the molecule must first be obtained.

Due to the unavailability of this data for EtA, we turned to the Hitchcock database, which provides photoabsorption data for ethanol (C_2H_5OH), the most structurally similar molecule to ethanolamine (Hitchcock & Mancini 1994). While minor differences in the exact resonance energies are expected, the overall absorption profile and the magnitude of the cross-section should be comparable. This similarity arises from both molecules featuring two carbon atoms in a fully saturated environment and the presence of an alcohol group. The data from ethanol thus serves as a reasonable proxy for estimating the photoabsorption characteristics of EtA in the C1s resonance edge.

Assuming a negligible fluorescence yield, owing to the low atomic numbers of carbon, oxygen, and nitrogen (Chen, Crasemann & Mark 1981), and a minimal production of anionic fragments within the investigated photon energy range, it is reasonable to consider that all absorbed photons contribute to cation formation. Under this assumption, the $\sigma_{\text{ph-i}}$ and $\sigma_{\text{ph-d}}$ cross-sections for EtA can be calculated as follows:

$$\sigma_{\text{ph-i}} = \frac{PIY_{\text{EtA}^+}}{100} \times \sigma_{\text{ph-abs}} \tag{2}$$

$$\sigma_{\text{ph-d}} = \left[1 - \frac{PIY_{\text{EtA}^+}}{100}\right] \times \sigma_{\text{ph-abs}}. \tag{3}$$

In these equations, PIY_{EtA^+} is the partial ion yield of the parent ion (EtA^+). These expressions provide a straightforward method to estimate the respective cross-sections based on the experimental data.

The calculated values for each X-ray energy are presented in Table 2, and a graphical representation depicting the behaviour of $\sigma_{\text{ph-d}}$ and $\sigma_{\text{ph-i}}$ with respect to the photon energy is shown in Fig. 5.

The $\sigma_{\text{ph-d}}$ values range from 2.01×10^{-18} cm^2 at 310.0 eV to 3.63×10^{-18} cm^2 at 295.0 eV, while the $\sigma_{\text{ph-i}}$ values are approxi-

Table 2. Absolute photoabsorption ($\sigma_{\text{ph-abs}}$), photodissociation ($\sigma_{\text{ph-d}}$), and photoionization ($\sigma_{\text{ph-i}}$) cross-sections of EtA at selected X-ray photon energies. The values of $\sigma_{\text{ph-abs}}$ were estimated using photoabsorption data from ethanol (taken from Hitchcock & Mancini 1994), and $\sigma_{\text{ph-d}}$ and $\sigma_{\text{ph-i}}$ were calculated using equations (2) and (3), respectively. The cross-section values are provided in units of cm^2.

Energy (eV)	$\sigma_{\text{ph-abs}}$ (cm^2)	$\sigma_{\text{ph-d}}$ (cm^2)	$\sigma_{\text{ph-i}}$ (cm^2)
288.5	3.54×10^{-18}	3.50×10^{-18}	3.87×10^{-20}
295.0	3.67×10^{-18}	3.63×10^{-18}	4.34×10^{-20}
297.5	3.01×10^{-18}	2.98×10^{-18}	3.66×10^{-20}
300.0	2.68×10^{-18}	2.66×10^{-18}	2.51×10^{-20}
305.0	2.28×10^{-18}	2.25×10^{-18}	2.47×10^{-20}
310.0	2.04×10^{-18}	2.01×10^{-18}	2.22×10^{-20}

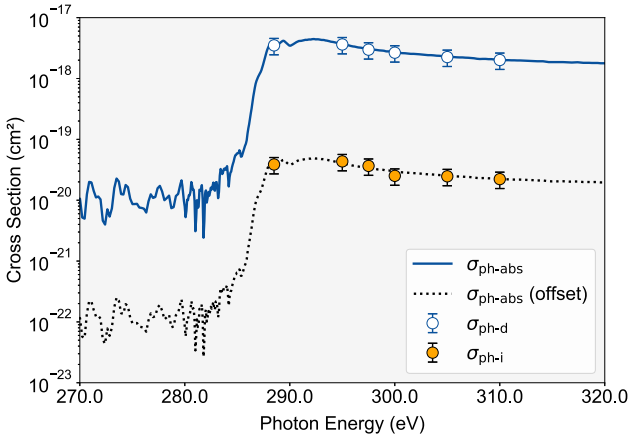

Figure 5. Photon energy dependence of the absolute photoabsorption ($\sigma_{\text{ph-abs}}$, solid blue line), photodissociation ($\sigma_{\text{ph-d}}$; upper, white circles), and photoionization ($\sigma_{\text{ph-i}}$; bottom, orange circles) cross-sections for EtA. The dotted black lines represent an offset of the photoabsorption cross-section for visual clarity. Photoabsorption data were approximated from ethanol as a proxy (taken from Hitchcock & Mancini 1994). The estimated error margin for the cross-section values is approximately 30 per cent.

mately 2 orders of magnitude lower, ranging from 2.22×10^{-20} cm^2 at 310.0 eV to 4.34×10^{-20} cm^2 at 295.0 eV. These cross-section values provide a basis for estimating the photodissociation rates of ethanolamine in various astrophysical environments, assuming the X-ray flux in those regions is known.

3.5 Survival of EtA in Sgr B2

Sgr B2, which hosts G+0.693−0.027 – the source where EtA was detected – is a massive and dense molecular cloud complex in the CMZ. It is situated 107 pc in projected distance from the supermassive black hole Sgr A* at the Galactic Centre (Schwörer et al. 2019), approximately 8.34 kpc from Earth (Reid et al. 2014). Sgr B2 is well-known for its time-varying Fe Kα fluorescence line at 6.4 keV and its hard X-ray continuum (Rogers et al. 2022), signatures that have led to its classification as an X-ray reflection nebula (Sunyaev, Markevitch & Pavlinsky 1993; Koyama et al. 1996). The cloud's large molecular mass ($7 \times 10^6 \text{M}_\odot$; Goldsmith et al. 1990; Schmiedeke et al. 2016) and high densities ($n_{\text{H}_2} \approx 10^3$–$10^6$ cm^{-3}; Schwörer et al. 2019) make it a critical site for investigating both star-formation processes and the impact of energetic phenomena in the Galactic Centre.

Despite the currently quiescent state of Sgr A* ($\sim 10^{33}$–10^{34} erg s^{-1}), multiple lines of evidence suggest that this supermassive black hole experienced much higher X-ray luminosities ($\gtrsim 10^{39}$ erg s^{-1}) in the recent past, on time-scales of tens to hundreds of years (Revnivtsev et al. 2004; Terrier et al. 2010, 2018; Rogers et al. 2022). X-ray flares from Sgr A*, once significantly brighter, are believed to have illuminated Sgr B2, producing the observed time-dependent Kα emission as the radiation propagates through the cloud. Owing to the 107 pc separation between the two objects, changes in the Sgr A* output can take years to decades to manifest at Sgr B2 (Clavel et al. 2013). In addition, cosmic rays have also been proposed as contributors to the X-ray emission and chemistry within Sgr B2, although the time variability of the Fe Kα line strongly suggests a dominant contribution from X-ray reflection (Rogers et al. 2022).

When estimating the half-lives of molecules like EtA under these energetic conditions, one must consider the attenuation of radiation caused by both dust grains and gas-phase molecules. Given the high column densities ($\sim 10^{23}$–10^{24} cm^{-2}; Terrier et al. 2010) and the complex composition of Sgr B2, we adopt an optical depth (τ_X) of 10 for X-rays in the relevant energy range. While the cloud is essentially opaque ($\tau_X \gg 1$) at lower energies (Henke, Gullikson & Davis 1993) and only marginally thick ($\tau_X \sim 1$) at higher energies (e.g. 6–7 keV), setting $\tau_X = 10$ provides a practical intermediate approximation for partially attenuated X-rays that still penetrate into denser regions. This choice aligns with models of X-ray-dominated regions (XDRs) where partial shielding is crucial to preserve COMs while enabling dissociation of outer-layer molecules (Maloney, Hollenbach & Tielens 1996). Balancing the complete shielding scenario (which would overestimate molecular half-lives) against negligible attenuation (which would underestimate them) ensures that the photodestruction rates for COMs are neither significantly overestimated nor underestimated, facilitating a consistent comparison of X-ray-induced chemistry-and the corresponding half-lives-across various regions of the cloud.

The determination of molecular photodissociation cross-sections ($\sigma_{\text{ph-d}}$) is crucial for estimating molecular abundances in interstellar and circumstellar environments. The depletion of a molecule subjected to a radiation field in the photon energy range $E_1 - E_2$ within a gaseous dusty cloud can be expressed as (Cottin, Moore & Benilan 2003; Boechat-Roberty et al. 2009):

$$-\frac{\text{d}N}{\text{d}t} = N k_{\text{ph-d}}, \tag{4}$$

where N is the column density (cm^{-2}) and $k_{\text{ph-d}}$ is the photodissociation rate (s^{-1}), defined as:

$$k_{\text{ph-d}} = \int_{E_1}^{E_2} \sigma_{ph-d}(E) F_X(E) \text{d}E, \tag{5}$$

where $F_X(E)$ is the X-ray photon flux (photons cm^{-2} eV^{-1} s^{-1}, both as functions of the photon energy ($E = h\nu$).

The half-life of a molecule, $t_{1/2}$, under these conditions can be determined using the relation (Monfredini et al. 2019):

$$t_{1/2} = \frac{\ln 2}{k_{\text{ph-d}}}. \tag{6}$$

Similarly, the photoionization rate ($k_{\text{ph-i}}$) can be calculated as:

$$k_{\text{ph-i}} = \int_{E_1}^{E_2} \sigma_{phi}(E) F_X(E) \text{d}E. \tag{7}$$

Table 3. Photodissociation rates $k_{\text{ph-d}}$, photoionization rates $k_{\text{ph-i}}$, and half-lifetimes $t_{1/2}$ for ethanolamine (EtA), formic acid (HCOOH), methyl formate ($HCOOCH_3$), and acetic acid (CH_3COOH). Calculations assume an X-ray luminosity of $L_X = 10^{39}$ erg s^{-1}, a distance $r = 107$ pc, and an optical depth $\tau_X = 10$. The results provide a comparative framework for assessing the stability of these molecules under the X-ray conditions of Sgr B2.

Molecule	$k_{\text{ph-d}}$ (s^{-1})	$k_{\text{ph-i}}$ (s^{-1})	$t_{1/2}$ (yr)
Ethanolamine	1.85×10^{-15}	1.05×10^{-17}	1.86×10^{7}
Formic acid	2.26×10^{-16}	1.20×10^{-17}	8.94×10^{7}
Methyl formate	1.44×10^{-15}	1.64×10^{-17}	1.52×10^{7}
Acetic acid	8.10×10^{-16}	2.16×10^{-17}	2.71×10^{7}

To determine the X-ray photon flux $F_X(E)$ at a specific location within a cloud like Sgr B2, we use the expression:

$$F_X = \frac{L_X}{4\pi r^2 h\nu} e^{-\tau_X}, \tag{8}$$

where L_X is the X-ray luminosity (erg s^{-1}) integrated over the photon energy range of interest, r is the distance from the X-ray source to the target position (cm), and τ_X is the X-ray optical depth. This formulation enables the determination of both photodissociation and photoionization rates for COMs, providing a framework for estimating their survival times under the influence of X-ray fields in dense molecular clouds.

For Sgr B2, we adopt $L_X = 10^{39}$ erg s^{-1}, corresponding to a distance $r = 3.3 \times 10^{20}$ cm, $\tau_X = 10$, and for EtA we consider the photon energy range from 288.5 to 310 eV. The computed $k_{\text{ph-d}}$, $k_{\text{ph-i}}$, and $t_{1/2}$ values for EtA are then compared with those previously reported for formic acid (HCOOH; Boechat-Roberty et al. 2005), methyl formate ($HCOOCH_3$; Fantuzzi et al. 2011), and acetic acid (CH_3COOH; Pilling et al. 2006).

It is important to note that the photodissociation lifetimes reported in this study are derived exclusively from measurements in the 288–310 eV range, corresponding to the C1s ionization region. Due to the technical limitations of the TGM beamline (which operates from 3 to 330 eV), our experimental data do not extend to higher energies where the ionization thresholds of nitrogen (ca. 400 eV) and oxygen (ca. 530 eV) occur. Since EtA contains both nitrogen and oxygen, its ionization cross-sections are expected to be significantly enhanced near these resonances. Therefore, the lifetimes presented here should be regarded as valid only within the C1s energy interval. Nonetheless, because all species were measured under comparable conditions, our comparisons remain robust. Future experiments extending to a broader energy range will be essential for determining the absolute lifetimes under a more realistic astrophysical X-ray spectrum.

Table 3 summarizes the calculated $k_{\text{ph-d}}$, $k_{\text{ph-i}}$, and $t_{1/2}$ values for all four molecules. Additionally, a bar plot of their $t_{1/2}$ values is presented in Fig. 6, providing a clear comparison of their relative stability under the X-ray field conditions characteristic of Sgr B2.

From the data shown in Table 3 and Fig. 6, the computed half-lifetimes of the molecules under the adopted X-ray field conditions in Sgr B2, expressed in units of 10^7 yr, are 1.86 (EtA), 8.94 (HCOOH), 1.52 ($HCOOCH_3$), and 2.71 (CH_3COOH), respectively. Formic acid stands out with a half-life roughly four times longer than the other molecules, likely due to its smaller size and simpler fragmentation pathways, which reduce its vulnerability to dissociation. Ethanolamine, despite being a fully saturated and relatively complex molecule, displays a half-life of the same order of magnitude as the other COMs, indicating similar resilience under the adopted X-ray conditions.

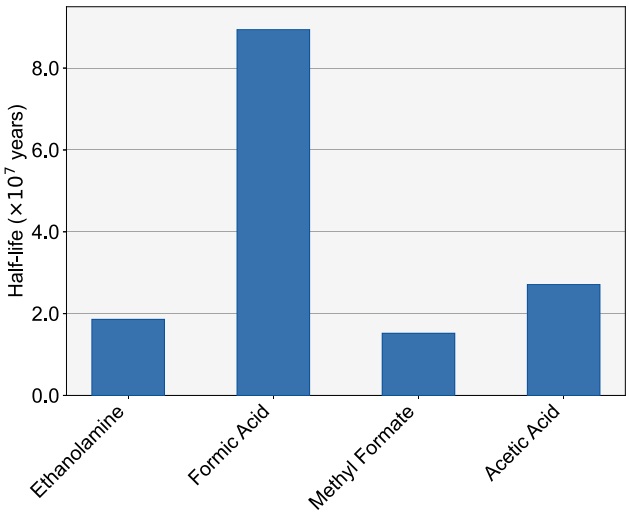

Figure 6. Comparison of half-lifetimes ($t_{1/2}$) for ethanolamine (EtA), formic acid (HCOOH), methyl formate ($HCOOCH_3$), and acetic acid (CH_3COOH) under X-ray field conditions characteristic of Sgr B2. Calculations assume an X-ray luminosity of 10^{39} erg s^{-1}, a distance $r = 107$ pc, and an optical depth $\tau_X = 10$. The bar plot highlights the relative stability of these molecules, illustrating the protective effect of high optical depths in dense molecular cloud environments.

These half-lives, on the order of 10^7 yr, highlight the protective effect of significant X-ray attenuation in dense molecular clouds like Sgr B2, where high column densities and dust mitigate the destructive impact of intense radiation fields. However, it is important to note that photodestruction half-lives alone do not necessarily correlate with observed molecular abundances. For example, acetic acid is typically less abundant than methyl formate, despite having a longer computed half-life. This discrepancy reflects the critical role of formation pathways and reaction kinetics in shaping molecular abundances. Methyl formate benefits from efficient gas-phase and grain-surface synthesis mechanisms, making it a commonly observed COM, while the formation routes of acetic acid are less favorable under typical interstellar conditions.

Furthermore, it should be noted that the lifetimes reported here reflect only the gas-phase behaviour of EtA and the other molecules considered. In dense environments such as Sgr B2, adsorption on to dust grains can significantly alter photodestruction dynamics. Within ice mantles, the generation of secondary species – such as radicals and photoelectrons – may enhance the destruction of adsorbed molecules. These solid-phase processes are not addressed in the present study and would require dedicated experiments to assess their contribution under astrophysically relevant conditions – such investigations are currently in progress within our group.

Complementary to this analysis, we also considered extreme values of optical depth, such as $\tau_X = 1$ and $\tau_X = 100$, to gain a more comprehensive understanding of the effects under different conditions. However, the results obtained were discarded, as they yielded half-lives on the order of only a few years or extremely long time-scales that cannot be realistically considered. These results emphasize the delicate balance between molecular formation and destruction processes in shaping the chemistry of dense molecular clouds, as well as illustrate the role of environmental factors such as radiative attenuation in preserving complex organic molecules in astrophysical environments.

4 CONCLUSIONS

In summary, our investigation combined experimental and computational approaches to investigate the photodissociation and photoionization dynamics of ethanolamine (EtA) under UV and soft X-ray photon fields. Through the use of synchrotron radiation to measure the PIYs of EtA and its fragments, we determined key photodestruction parameters such as the photodissociation and photoionization cross-sections. These data, combined with estimates of the absolute photoabsorption cross-section of EtA, enabled us to calculate photodissociation rates and half-lifetimes for the molecule under astrophysically relevant X-ray field conditions, specifically those characteristic of the Sgr B2 molecular cloud.

Our experiments revealed that EtA fragments predominantly at m/q = 30, corresponding to $CH_2NH_2^+$, a highly stable nitrogen-containing cation. This finding aligns with the results of BOMD simulations, which demonstrated a preference for initial C–C bond cleavage followed by charge localization on the nitrogen-bearing fragment. Although $CH_2NH_2^+$ has not yet been detected in the ISM, its stability and its prevalence in the dissociation of EtA support its potential relevance in interstellar chemistry. $CH_2NH_2^+$ stands out as a promising target for future astronomical observations, particularly in regions where ethanolamine and related alkylamine systems have already been identified. Other notable fragments include m/q = 28, m/q = 29, m/q = 31, and m/q = 42, which our computations predominantly attributed to $HCNH^+$, CH_2NH^+, CH_2OH^+, and $H_2CCNH_2^+$, respectively. These results reveal a strong dominance of nitrogen-containing ions, highlighting the central role of the nitrogen atom in determining dissociation pathways.

In the soft X-ray regime, the fragmentation patterns of EtA revealed increased production of lighter ions and a reduction in the parent ion's survivability compared to UV energies. Despite this, our results demonstrate that EtA exhibits significant resilience under the intense X-ray fields of Sgr B2, with a computed half-life of approximately 1.86×10^7 yr. This value is comparable to those of other COMs such as methyl formate (1.52×10^7 yr) and acetic acid (2.71×10^7 yr), underscoring its ability to persist in dense astrophysical environments. Formic acid, a simpler molecule, exhibited a much longer half-life (8.94×10^7 yr), likely due to its reduced fragmentation susceptibility. These findings highlight that molecular size, complexity, and fragmentation dynamics play critical roles in determining survival times under astrophysical conditions.

Our results also emphasize the significance of X-ray attenuation in preserving COMs in regions like Sgr B2. The adopted optical depth ($\tau = 10$) reflects the dense, dusty nature of the cloud, which shields molecules from rapid destruction. Without such attenuation, half-lives would be reduced to hundreds or thousands of years, precluding the accumulation of molecules like EtA in these environments. This protective effect is critical for understanding the chemical evolution of dense molecular clouds and the potential delivery of prebiotic molecules to nascent planetary systems.

Our study further illustrates that photodissociation half-lives alone cannot fully explain observed molecular abundances. For example methyl formate is more abundant than acetic acid in interstellar environments, despite its shorter half-life. This discrepancy highlights the importance of formation pathways and reaction kinetics. Such insights are crucial for developing comprehensive models of interstellar chemistry, where the interplay between formation and destruction processes ultimately governs the distribution of complex molecules.

ACKNOWLEDGEMENTS

The authors thank MSc Sergio A. Guerrero-Pardo for his valuable discussions, as well as Dr Sergio Pilling and the staff of the Brazilian Synchrotron Light Laboratory (LNLS) for their assistance during the experiments. This manuscript is based on work from the COST Action CA20129 – Multiscale Irradiation and Chemistry Driven Processes and Related Technologies (MultIChem), supported by COST (European Cooperation in Science and Technology). We thank the supplementary financial support from the University of Kent and The Center for Astrochemical Studies at the Max Planck Institute for Extraterrestrial Physics (CAS@MPE). Partial funding for this work, provided by Universidad de Antioquia via 'Estrategia para la sostenibilidad', is acknowledged.

DATA AVAILABILITY

The data underlying this work will be shared on reasonable request to the corresponding author.

REFERENCES

Abplanalp M. J., Kaiser R. I., 2019, Phys. Chem. Chem. Phys., 21, 16949
Anicich V. G., 1993, J. Phys. Chem. Ref. Data, 22, 1469
Ásgeirsson V., Bauer C. A., Grimme S., 2017, Chem. Sci., 8, 4879
Bakovic M., Fullerton M. D., Michel V., 2007, Biochem. Cell Biol., 85, 283
Bannwarth C., Caldeweyher E., Ehlert S., Hansen A., Pracht P., Seibert J., Spicher S., Grimme S., 2021, WIREs Comput. Mol. Sci., 11, e1493
Bannwarth C., Ehlert S., Grimme S., 2019, J. Chem. Theory Comput., 15, 1652
Bauer C. A., Grimme S., 2016, J. Phys. Chem. A, 120, 3755
Bennett C. J., Kaiser R. I., 2007, ApJ, 661, 899
Bernstein M. P., Dworkin J. P., Sandford S. A., Cooper G. W., Allamandola L. J., 2002, Nature, 416, 401
Biancalani S., Corazzi M. A., Rivilla V. M., Brucato J. R., 2024, A&A, 691, A256
Boechat-Roberty H. M., Neves R., Pilling S., Lago A. F., de Souza G. G. B., 2009, MNRAS, 394, 810
Boechat-Roberty H. M., Pilling S., Santos A. C. F., 2005, A&A, 438, 915
Bonfim V. S. A., Souza C. P., de Oliveira D. A. B., Baptista L., Santos A. C. F., Fantuzzi F., 2024, J. Chem. Phys., 160, 124308
Budin I., Szostak J. W., 2011, Proc. Natl. Acad. Sci., 108, 5249
Burmeister F. et al., 2010, J. Electron Spectros. Relat. Phenomena, 180, 6
Burton A. S., Stern J. C., Elsila J. E., Glavin D. P., Dworkin J. P., 2012, Chem. Soc. Rev., 41, 5459
Busch L. A., Belloche A., Garrod R. T., Müller H. S. P., Menten K. M., 2022, A&A, 665, A96
Cable M. L., Vu T. H., Maynard-Casely H. E., Choukroun M., Hodyss R., 2018, ACS Earth Space Chem., 2, 366
Cardozo T. M., De Sousa D. W. O., Fantuzzi F., Nascimento M. A. C., 2024, in Yáñez M., Boyd R. J., eds, Comprehensive Computational Chemistry, 1st edn. Elsevier, Oxford, p. 552
Cavasso Filho R., Homem M., Landers R., de Brito A. N., 2005, J. Electron Spectros. Relat. Phenomena, 144, 1125
Cavasso Filho R., Lago A., Homem M., Pilling S., Naves de Brito A., 2007, J. Electron Spectros. Relat. Phenomena, 156, 168
Chen M. H., Crasemann B., Mark H., 1981, Phys. Rev. A, 24, 177
Clavel M., Terrier R., Goldwurm A., Morris M. R., Ponti G., Soldi S., Trap G., 2013, A&A, 558, A32
Cottin H., Moore M. H., Benilan Y., 2003, ApJ, 590, 874
Cuppen H. M., Linnartz H., Ioppolo S., 2024, Annu. Rev. A&A, 62, 243
de Oliveira G., Martin J. M. L., Silwal I. K. C., Liebman J. F., 2001, J. Comput. Chem., 22, 1297
de Sousa D. W. O., Nascimento M. A. C., 2017, Acc. Chem. Res., 50, 2264
de Sousa D. W. O., Nascimento M. A. C., 2019, Phys. Chem. Chem. Phys., 21, 13319

Eckhardt A. K., Bergantini A., Singh S. K., Schreiner P. R., Kaiser R. I., 2019, Angew. Chem. Int. Ed., 58, 5663
Ehrenfreund P., Charnley S. B., 2001, in Exo-/Astro-biology: Proc. First European Workshop. ESA Publications Division, Noordwijk, p. 35
Elsila J. E., Dworkin J. P., Bernstein M. P., Martin M. P., Sandford S. A., 2007, ApJ, 660, 911
Facchini L., Losito I., Cianci C., Cataldi T. R. I., Palmisano F., 2016, Electrophoresis, 37, 1823
Fantuzzi F., Pilling S., Santos A. C. F., Baptista L., Rocha A. B., Boechat-Roberty H. M., 2011, MNRAS, 417, 2631
Fantuzzi F., Rudek B., Wolff W., Nascimento M. A. C., 2018, J. Am. Chem. Soc., 140, 4288
Fantuzzi F., Wolff W., Quitián-Lara H. M., Boechat-Roberty H. M., Hilgers G., Rudek B., Nascimento M. A. C., 2019, Phys. Chem. Chem. Phys., 21, 24984
Garrod R. T., Weaver S. L. W., Herbst E., 2008, ApJ, 682, 283
Gerakines P., Moore M., Hudson R., 2004, Icarus, 170, 202
Glavin D. P. et al., 2010, Meteorit. Planet. Sci., 45, 1695
Glavin D. P., Elsila J. E., Burton A. S., Callahan M. P., Dworkin J. P., Hilts R. W., Herd C. D. K., 2012, Meteorit. Planet. Sci., 47, 1347
Goldsmith P. F., Lis D. C., Hills R., Lasenby J., 1990, ApJ, 350, 186
Henke B., Gullikson E., Davis J., 1993, At. Data Nucl. Data Tables, 54, 181
Hitchcock A., Mancini D., 1994, J. Electron Spectros. Relat. Phenomena, 67, 1
Holtom P. D., Bennett C. J., Osamura Y., Mason N. J., Kaiser R. I., 2005, ApJ, 626, 940
Huntress W. T., Elleman D. D., 1970, J. Am. Chem. Soc., 92, 3565
Ioppolo S. et al., 2020, Nat. Astron., 5, 197
Kechoindi S., Ben Yaghlane S., Mogren Al Mogren M., Bodi A., Hochlaf M., 2024, Phys. Chem. Chem. Phys., 26, 24656
Kleimeier N. F., Eckhardt A. K., Kaiser R. I., 2021, J. Am. Chem. Soc., 143, 14009
Knowles D. J., Wang T., Bowie J. H., 2010, Org. Biomol. Chem., 8, 4934
Koopman J., Grimme S., 2019, ACS Omega, 4, 15120
Koopman J., Grimme S., 2021 J. Am. Soc. Mass Spectrom., 32, 1735
Koyama K., Maeda Y., Sonobe T., Takeshima T., Tanaka Y., Yamauchi S., 1996, PASJ, 48, 249
Krysenko S. et al., 2019, MBio, 10, e00326
Leclerc J. C., Lorquet J. C., 1967, J. Phys. Chem., 71, 787
Linnartz H., Ioppolo S., Fedoseev G., 2015, Int. Rev. Phys. Chem., 34, 205
Londoño-Restrepo J., Gómez S., Quitián-Lara H. M., Fantuzzi F., Restrepo A., 2025, Chem. Sci. 16, 3051
Maloney P. R., Hollenbach D. J., Tielens A. G. G. M., 1996, ApJ, 466, 561
Marks J. H., Wang J., Sun B.-J., McAnally M., Turner A. M., Chang A. H.-H., Kaiser R. I., 2023, ACS Central Sci., 9, 2241
Markus C. R., Thorwirth S., Asvany O., Schlemmer S., 2019, Phys. Chem. Chem. Phys., 21, 26406
Massalkhi S. et al., 2023, A&A, 678, A45
Millar T. J., Walsh C., Van de Sande M., Markwick A. J., 2024, A&A, 682, A109
Molder U., Pikver R., Koppel I., 1983, Org. React. (Tartu), 20, 355
Monfredini T., Fantuzzi F., Nascimento M. A. C., Wolff W., Boechat-Roberty H. M., 2016, ApJ, 821, 4
Monfredini T. et al., 2019, MNRAS, 488, 451
Monnard P., Deamer D. W., 2002, Anat. Rec., 268, 196
Muller G., Voronova K., Sztáray B., Meloni G., 2016, J. Phys. Chem. A, 120, 3906
Muñoz Caro G. M., Ciaravella A., Jiménez-Escobar A., Cecchi-Pestellini C., González-Díaz C., Chen Y.-J., 2019, ACS Earth Space Chem., 3, 2138
Nandedkar A. K., 1974, Biochem. Med., 11, 67
Nandedkar A. K., 1975, Biochem. Med., 12, 116
Okada S., Abe Y., Taniguchi S., Yamabe S., 1987, J. Am. Chem. Soc., 109, 295
Pilling S., Andrade D. P. P., da Silveira E. F., Rothard H., Domaracka A., Boduch P., 2012, MNRAS, 423, 2209
Pilling S., Santos A. C. F., Boechat-Roberty H. M., 2006, A&A, 449, 1289
Quitián-Lara H. M., Fantuzzi F., Oliveira R. R., Nascimento M. A. C., Wolff W., Boechat-Roberty H. M., 2020, MNRAS, 499, 6066
Ramachandran R. et al., 2024, ApJ, 975, 181
Reid M. J. et al., 2014, ApJ, 783, 130
Revnivtsev M. G. et al., 2004, A&A, 425, L49
Richardson V. et al., 2024, Phys. Chem. Chem. Phys., 26, 22990
Rivilla V. M. et al., 2021, Proc. Natl. Acad. Sci., 118, e2101314118
Rogers F., Zhang S., Perez K., Clavel M., Taylor A., 2022, ApJ, 934, 19
Sandford S. A., Nuevo M., Bera P. P., Lee T. J., 2020, Chem. Rev., 120, 4616
Schmiedeke A. et al., 2016, A&A, 588, A143
Schneiker A., Góbi S., Joshi P. R., Bazsó G., Lee Y.-P., Tarczay G., 2021, J. Phys. Chem. Lett., 12, 6744
Schwörer A. et al., 2019, A&A, 628, A6
Shimajiri T., Kawaguchi S., Suzuki T., Ishigaki Y., 2024, Nature, 634, 347
Shukla S. D., Turner J. M., 1980, Biochem. J., 186, 13
Singh P. C., Shen L., Zhou J., Schlegel H. B., Suits A. G., 2010, ApJ, 710, 112
Sorrell W. H., 2001, ApJ, 555, L129
Sunyaev R. A., Markevitch M., Pavlinsky M., 1993, ApJ, 407, 606
Suzuki T., Ohishi M., Hirota T., Saito M., Majumdar L., Wakelam V., 2016, ApJ, 825, 79
Terrier R. et al., 2010, ApJ, 719, 143
Terrier R., Clavel M., Soldi S., Goldwurm A., Ponti G., Morris M. R., Chuard D., 2018, A&A, 612, A102
Thackston R., Fortenberry R. C., 2018, Icarus, 299, 187
Turner A. M. et al., 2018, Nat. Commun., 9, 3851
Vuitton V., Doussin J., Benilan Y., Raulin F., Gazeau M., 2006a, Icarus, 185, 287
Vuitton V., Yelle R. V., Anicich V. G., 2006b, ApJ, 647, L175
Wang J. et al., 2024, J. Am. Chem. Soc., 146, 28437
William E., 2025, NIST Chemistry WebBook, NIST Standard Reference Database, 69
Yelle R. V., Vuitton V., Lavvas P., Klippenstein S. J., Smith M. A., Hörst S. M., Cui J., 2010, Faraday Discuss., 147, 31
Yuen C. H., Ayouz M. A., Balucani N., Ceccarelli C., Schneider I. F., Kokoouline V., 2019, MNRAS, 484, 659
Zeng S. et al., 2018, MNRAS, 478, 2962
Zeng S. et al., 2020, MNRAS, 497, 4896
Zeng S. et al., 2021, ApJ, 920, L27
Zhang C., Wang J., Turner A. M., Marks J. H., Chandra S., Fortenberry R. C., Kaiser R. I., 2023, ApJ, 952, 132
Zhang J. et al., 2024, MNRAS, 533, 826
Zhang X., Tian G., Gao J., Han M., Su R., Wang Y., Feng S., 2017, Orig. Life Evol. Biosph., 47, 413

This paper has been typeset from a TEX/LATEX file prepared by the author.